Numerical and experimental evaluation of TPMS Gyroid scaffolds for bone tissue engineering

A. P. G. Castro, R. B. Ruben, S. B. Gonçalves, J. Pinheiro, J. M. Guedes & P. R. Fernandes

Taylor & Francis
Taylor & Francis Group

Check for updates

Numerical and experimental evaluation of TPMS Gyroid scaffolds for bone tissue engineering

A. P. G. Castro[a] , R. B. Ruben[b] , S. B. Gonçalves[a], J. Pinheiro[a], J. M. Guedes[a] and P. R. Fernandes[a]

[a]IDMEC, Instituto Superior Técnico, Universidade de Lisboa, Lisbon, Portugal; [b]ESTG, CDRSP, Polytechnic Institute of Leiria, Leiria, Portugal

ABSTRACT

The combination of computational methods with 3D printing allows for the control of scaffolds microstructure. Lately, triply periodic minimal surfaces (TPMS) have been used to design porosity-controlled scaffolds for bone tissue engineering (TE). The goal of this work was to assess the mechanical properties of TPMS Gyroid structures with two porosity levels (50 and 70%). The scaffold stiffness function of porosity was determined by the asymptotic homogenisation method and confirmed by mechanical testing. Additionally, microCT analysis confirmed the quality of the printed parts. Thus, the potential of both design and manufacturing processes for bone TE applications is here demonstrated.

1. Introduction

In biomechanics and biomedical engineering, scaffolds can be defined as porous structures that act as cellular support for the growth of new tissue (Boccaccio 2011). For tissue engineering (TE) applications, scaffolds shall permit the diffusion of oxygen, nutrients and metabolic waste, in order to ensure adequate cellular growth and proliferation (Olivares & Lacroix 2012; Rahbari et al. 2016). In the specific case of bone TE, the structural integrity of the scaffolds is also important to enhance bone shape and function during and after the regeneration and remodelling processes (Rodrigues et al. 2011; Papantoniou et al. 2014; Barabaschi & Manoharan 2015). This means that there is a need for scaffolds to be optimized for appropriate porosity, permeability and mechanical properties (e.g., stiffness, viscosity or compressibility) (Bobbert et al. 2017).

Different techniques have been studied for the development of new TE scaffolds, from optimization to top-down or bottom-up approaches (Lu et al. 2013). Among them, the development of scaffolds based on the triply periodic minimal surfaces (TPMS) method has shown to enhance cell migration while retaining a high degree of mechanical and structural rigidity (Yoo 2014). Moreover, the resulting geometries are suitable to be produced by additive manufacturing (Bobbert et al. 2017; Feng et al. 2018). TPMS are defined mathematically as infinite and periodic surface curvatures, which allow for fully controllable homogenous scaffold projects, parting from the design of the repeatable unit cell (Gauvin et al. 2012; Bobbert et al. 2017; Montazerian et al. 2017). Some of the existent TPMS scaffolds types are Schwartz D, Schwartz P or Gyroid (Rajagopalan & Robb 2006; Gauvin et al. 2012; Giannitelli et al. 2014; Blanquer et al. 2017).

As important as the development methods and target applications, scaffolds shall be produced with enough accuracy. This means that the designed structure shall correspond to the fabricated one, in order to promote the adequate cellular and tissue response after implantation (Castro & Lacroix 2018). 3D printing, electrospinning or selective laser sintering have been applied in scaffold manufacturing (Eshraghi & Das 2012; Lu et al. 2013; Wismer et al. 2014; Hollister et al. 2016). In the past, it has been found that produced scaffolds were different from the respective project and this raised concerns about the applicability of these devices in the biomedical industry (Hollister & Murphy 2011; Campos Marin & Lacroix 2015; Webber et al. 2015). 3D MultiJet printing, which is an additive manufacturing technique, has proven to be a good option for scaffold manufacture, benefiting from efficient cost control and high production accuracy (Castilho et al. 2011; Velasco et al. 2016).

Thus, this present study is focused on the design of scaffolds based on the TPMS method, with the

objective of evaluating the quality of 3D MultiJet printing for bone tissue applications, i.e., how does the manufacturing process affect the estimated or designed properties of the scaffolds.

TPMS Gyroid scaffolds were built in two porosity levels (50 and 70%), in order to assess their mechanical properties as function of porosity. Mechanical testing and numerical homogenisation were performed for this purpose. Also, MicroCT imaging was performed along with subsequent 3D modelling from image reconstruction, to evaluate the accuracy of both 3D printing and cleaning process (Castro & Lacroix 2018). This particular Gyroid type has been described by previous studies (Olivares & Lacroix 2012; Almeida & Bártolo 2014; Montazerian et al. 2017; Speirs et al. 2017) as having superior ability to promote cell differentiation and proliferation, when compared with other traditional geometrical arrangements. In addition, one of the major advantages of using TPMS Gyroid structures is related to their internal geometry, which allows for an efficient removal of all the support material necessary for 3D MultiJet printing. This procedure is not as straightforward in other TPMS structures, i.e., it is important to note that for using MultiJet techniques, the geometry should consider paths large enough to allow wax draining from the interior of the scaffold (Sochol et al. 2016).

2. Materials and methods

This work is focused on the design, manufacturing and evaluation of TPMS Gyroid scaffolds with 50 and 70% porosity (ahead referred as G50 and G70, respectively). The selection of the porosity levels was based on the ability of the structure to allow for sufficient fluid flow through their interior, in order to allow for adequate cellular growth (O'Brien et al. 2007; Viana et al. 2013; Castro & Lacroix 2018).

2.1. Design and homogenisation

The scaffolds were created with a custom TPMS generator (Dinis et al. 2014), which deals with the mathematical development of the structure as a function of the designed porosity and also with the STL file export. This generator uses the Gyroid mathematical functions to create scaffold surfaces with the designed porosity, which are then converted to a Finite Element (FE) mesh (please refer to Dinis et al. (2014) for further information). Depending on the number of elements per side on each single unit of the periodic scaffold, the porosity of this FE mesh may vary from the originally designed porosity. The FE mesh is the source for the numerical homogenisation and also for the STL file (for 3D printing). In this work, the TPMS generator was set to create 20 finite elements per side, as a compromise between accuracy and computational time.

The asymptotic homogenisation method described by Guedes and Kikuchi (Guedes & Kikuchi 1990) allows the calculation of the equivalent elastic coefficients for periodic porous structures with the homogenised properties E_{ijkm}^{H} given by:

$$E_{ijkm}^{H} = \frac{1}{Y} \int_{\yen} E_{pqrs} \left(\delta_{rk}\delta_{sm} - \frac{\partial \overline{\chi}_r^{km}}{\partial y_s} \right) \left(\delta_{pi}\delta_{qj} - \frac{\partial \overline{\chi}_p^{ij}}{\partial y_q} \right) dY \tag{1}$$

where $\overline{\chi}_r^{km}$ are the local deformation modes when the unit cell is subject to six unit average strains, E_{pqrs} are the elastic properties of the solid part (¥) of the cell Y, |Y| is the volume of the basic unit cell ($1 \times 1 \times 1$ mm) and δ_{ij} is the Kronecker delta.

2.2. 3D printing

The samples tested in the present work were printed in the Biomechanics Lab of Instituto Superior Técnico using ProJet 3D MJP 3600 (3D Systems, USA). Typically, 3D MultiJet printers have a resolution on the order of 10 μm, allowing its application in the development of intricated microstructures required in TE scaffolds (Melchels et al. 2011; Rahbari et al. 2016). The chosen material was Visijet M3 Crystal, as recommended by the manufacturer of the 3D MultiJet printer. The choice of this material is related to its properties, which presents a tabled Young's Modulus value of 1.46 GPa, similar to the values observed in trabecular bone, and it is certified with USP Class VI norm, allowing its use in several medical applications (3D Systems 2017). This technology also uses an additional support material to allow layer-by-layer construction that needs to be removed after the printing. For the present work, the commercial material Visijet S300 was used, again by recommendation of the manufacturer. The parts postprocessing followed the supplier specifications for USP Class VI application (3D Systems 2017), considering a first step in which the support material is melted in the ProJet Finisher oven (3D Systems, USA) at 60° C and several baths of 99%+ isopropyl alcohol to remove the residual support material.

The specimens were created in accordance with ASTM norm D695 - 02a (ASTM International 2002),
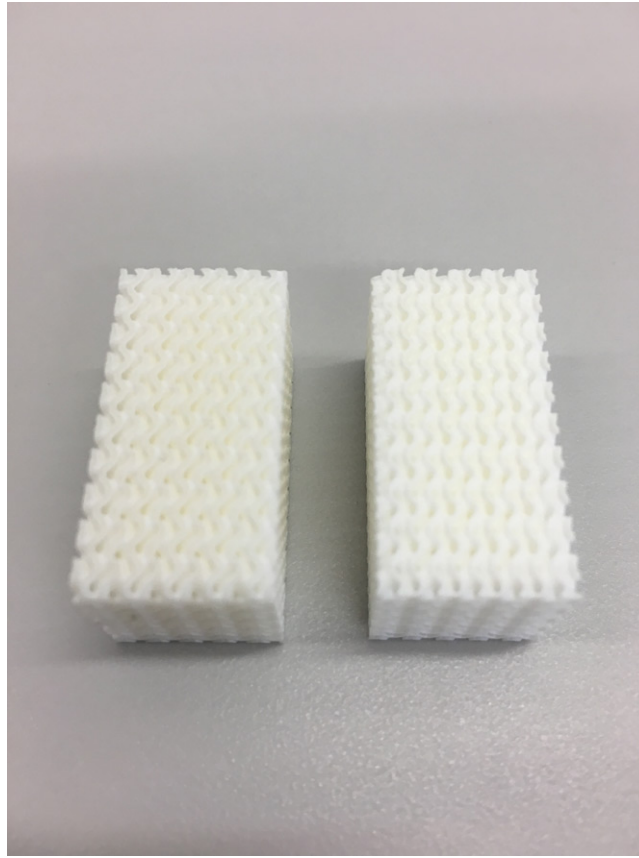
Figure 1. Printed specimens: G50 (left) and G70 (right) with 3 mm cell side.

which lead to parts with height that was double of their width, ideally with 12.7 × 12.7 × 25.4 mm. Additionally, the work of Coelho et al. (2015) stated that a minimum of five unit cells were necessary in each dimension to ensure the validity of the numerical procedures. Therefore, the final structures were built on 5 × 5 × 10 configuration with 2.5 mm (12.5 × 12.5 × 25) and 3 mm (15 × 15 × 30) unit cell side sizes (scaled from the original 1 mm). Figure 1 shows the printed parts of 3 mm.

Seven specimens of each porosity level and unit cell side size were printed for mechanical testing (more than the five specimens specified as the minimum by the norm), plus three samples of the G50 3 mm scaffold for microCT scanning (total of 31 specimens manufactured).

2.3. MicroCT scanning

To evaluate the accuracy of both 3D printing and cleaning process, three samples of the G50 3 mm scaffold (not mechanically tested) were scanned with microCT, using the equipment 1174 (Skyscan, USA). For all the three scans, a 26.32 μm precision was used between pixels and also between slices. Skyscan

machine generates a set of bmp 8-bits grayscale images (256 intensity levels from 0 to 255) one for each scanned slice. To compute scaffold porosity the set of images were segmented using Otsu global optimum threshold (Nyma et al. 2012; Balabanian et al. 2017). So, for each image slice the optimum intensity threshold (k^*) maximizes the between-class variance:

$$\sigma_B^2(k^*) = \frac{(m_G P_1 - m)^2}{P_1(1-P_1)} = \max_{0 \le k \le 255} \sigma_B^2(k) \qquad (2)$$

where m_G is the average intensity of all image, m is the average intensity until the level k, and P_1 is the sum of normalized histogram values until the level k. Figure 2 shows one typical example of the normalized histogram, since all slices present similar histograms, and the respective slice. With the segmentation of all slices is possible to compute the microCT porosity and generate a new STL file based on reverse engineering.

2.4. Mechanical testing

Following the homogenisation outputs, the mechanical properties of the printed scaffolds were evaluated using mechanical testing equipment, namely the
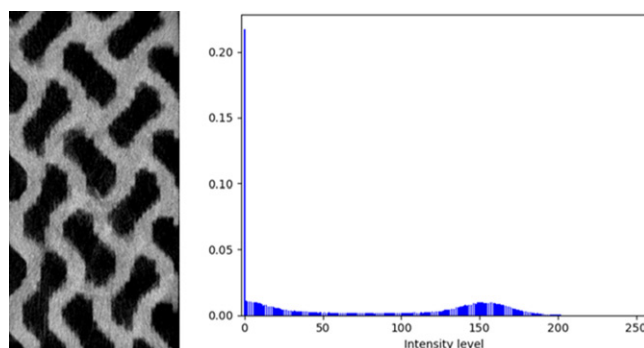
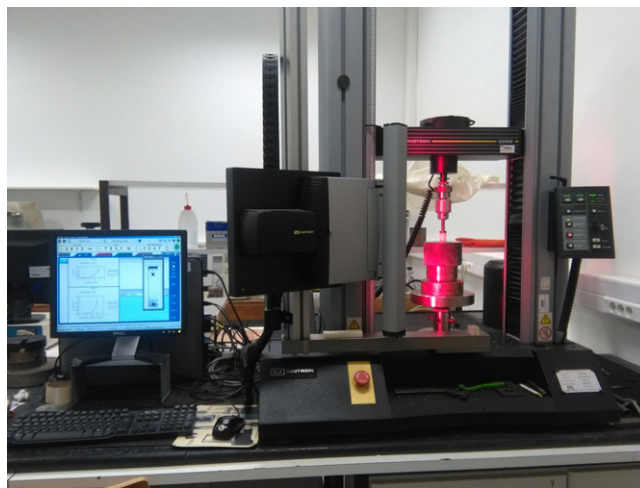**Figure 2.** Image slice (left) and the normalized histogram (right).

Figure 3. Experimental setup using an Instron 5566 and an Instron AVE.

Young's Module and tensile strength. The experimental data was acquired in LEM2 of Instituto Superior Técnico using an Instron® testing Machine 5566 (Instron, USA) equipped with a 10kN load cell and an Advanced Video Extensometer (AVE - Instron, USA). The experimental setup for typical uniaxial compression test until rupture is shown in Figure 3, being the testing speed set to 1.3 mm/min. Two methodologies were used to measure the specimen strain and consequently compute the scaffolds elastic properties: the testing machine arm ("ARM") and the video extensometer ("AVE"). The two experimental stiffness calculations were posteriorly compared with the numerical predictions from the homogenisation method ("HMG").

3. Results

3.1. MicroCT scanning

The three samples of the G50 3 mm scaffold scanned with microCT presented similar values of porosity (2.3% maximum difference). Table 1 also shows an average error between the original STL and the

Table 1. Porosity of G50 3 mm scaffold samples.

Sample	MicroCT (%)	Original STL (%)	TPMS generator (%)
1	53.9		
2	55.2	62.1	51.0
3	52.9		

manufactured scaffolds of approximately 8%. The original STL file sent to the 3D MultiJet printing had 62.1% porosity, while the designed porosity was 51% (from the TPMS generator software). Additionally, Figure 4 shows that it is possible to verify the manufactured scaffold structure, where is visible the correct Gyroid geometry with the designed holes connectivity.

3.2. Mechanical properties

Young's Modulus values were calculated from both experiments and numerical methods. Thus, Table 2 compares the experimental average values (ARM and AVE) from the seven samples with the numerical predictions from the homogenisation method (HMG) of Guedes and Kikuchi (Guedes & Kikuchi 1990). The standard deviation values from each experimental method are also presented. The last two columns
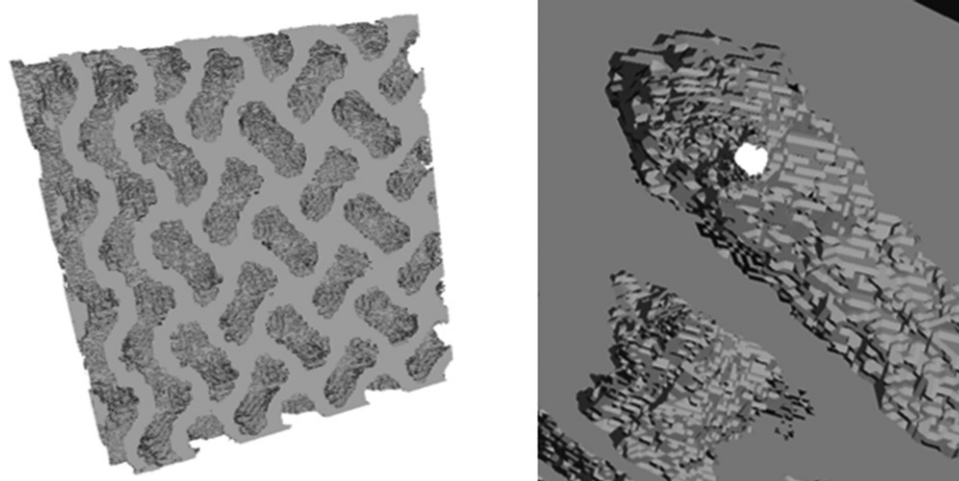
Figure 4. Generated STL from microCT images with a zoomed part.

Table 2. Experimental and numerical Young's Modulus values.

Cell side (mm)	Model	ARM (GPa)	AVE (GPa)	HMG (GPa)	Error HMG-ARM (%)	Error HMG-AVE (%)
2.5	G50	0.2485 ± 0.0068	0.2731 ± 0.0123	0.2296	8.23	18.95
	G70	0.1005 ± 0.0035	0.1086 ± 0.0029	0.1070	6.07	1.50
3	G50	0.2258 ± 0.0084	0.2622 ± 0.0110	0.2296	1.66	14.20
	G70	0.1004 ± 0.0036	0.0898 ± 0.0359	0.1070	6.17	16.07

present the difference (error) between the average values of each experimental method and the corresponding numerical predictions ("Error HMG-ARM" and "Error HMG-AVE").

For both cell side sizes, the ARM presented the lower Young's Modulus values, while the AVE recorded the higher ones. The average difference between the two experimental data sources was 10.5%, considering the four groups of samples tested. The numerical predictions HMG were closer to the values measured by the ARM in three out of four cases (5.5% average difference against 12.5% for HMG-AVE). In detail, the average HMG-ARM difference was 7% for 2.5 mm, decreasing to 3.5% for the 3 mm cell side parts. The maximum numerical-experimental difference was 19% (HMG-AVE, G50 2.5 mm), contrasting with the lowest difference found for HMG-AVE for G70 2.5 mm (1%).

The increase in porosity, for this Gyroid geometry, produced a considerable change in the stiffness of the structure: approximately 60% decrease for 2.5 mm parts and 56% for 3 mm parts, considering the ARM values. These values are aligned with the decrease in stiffness calculated by the homogenisation method, which was 53%. All the samples presented a shear failure mode.

4. Discussion

The relationship between Young's Modulus and porosity was in accordance with what was previously reported, i.e., higher stiffness for lower porosities, tending to values closer to the ones usually found in literature for trabecular bone (Rajagopalan & Robb 2006; Giannitelli et al. 2014; Lakatos et al. 2014; Velasco et al. 2016; Bobbert et al. 2017). The experimental results do not show relevant differences with the increase of the unit cell side size, from 2.5 mm to 3 mm, but this type of technology may be inadequate for very small pore sizes, as happens with other TPMS-based scaffolds. Some works in the literature reported the mechanical structures of several TPMS surfaces and different porosities; in what concerns to Gyroid scaffolds, the work of Kapfer et al. (2011) measured 0.233 GPa for 50% porosity, which is aligned with the results obtained in this work.

The average difference in the measurements from ARM and AVE was approximately 10.5% but increased from 2.5 to 3 mm cell side; the results from ARM were closer to the numerical predictions HMG than the equivalent AVE results. According to the instructions of the manufacturer, the AVE is not recommended for compression tests with specimens smaller than 50 mm, which may partially justify the larger error detected in the AVE results.

The viscosity of the support wax (recommended by the printer's manufacturer) made it difficult to remove through the small pores of these scaffolds. The removal of the support material is a delicate process and consequently the final aspect of the parts

may not reliable enough. In other words, although the precision of the printer used is around 16 μm, which is reflected in good accuracy in the physical representation of the designed part, the cleaning post-processing is manual and is presumably not efficient enough. As so, the presence of support material inside the parts means that the measurements are not reflecting the real elastic properties of the material, but the properties of the material plus the residual wax. The different porosities obtained with the microCT analysis are either due to this post-processing (incomplete or inefficient removal of the wax, so not directly related to the manufacturing process) or to the difference noted between the designed porosity (from the TPMS generator) and the porosity of the STL file (which was used to print the scaffolds).

This work only considered TPMS Gyroid scaffolds, which is a limitation. Further tests should be performed, considering other TPMS scaffolds and potentially other porosity levels, in order to establish more complete stiffness versus porosity trends. The microCT analysis was limited to 3 mm parts, but its results showed that the real porosity of the scaffolds was between the designed porosity from the TPMS generator software and the porosity of the STL file used as source by the 3D printer. This needs to be further assessed in future studies, but one possibility may be to increase the number of finite elements per side of each single unit, thus refining the models and eventually reducing the difference in porosity between STL and TPMS generator files. Additionally, the manufacturing material used in this work is not specific for bone TE scaffolds, even considering that it is certified with USP Class VI norm. Common materials for bone TE (e.g., PCL or PLLA) or hydroxyapatite coatings may be considered, if proved to be compatible with the available 3D MultiJet printer. With different (and more adequate) materials, biocompatibility of the printed scaffolds may also be evaluated, towards clinical translation.

5. Conclusions

This work shows that TPMS scaffolds can be produced by 3D MultiJet printing with significant accuracy. As so, it gives a good perspective over the crafting of scaffolds for bone TE applications, from their numerical development to the manufacturing. It was possible to assess that for this type of fabrication the design process should provide large enough pores to allow for the removal of the support material used during the printing process; this material has a high viscosity, which hinders its removal from very delicate microstructures.

Additionally, elasticity is one of the essential parameters to promote appropriate cellular growth and proliferation, and the homogenisation method used here proved to be correct on predicting the stiffness of the scaffolds as a function of porosity. However, the difference between numerical and experimental outputs needs to be reduced in further studies by refining the scaffold models from the initial design stage.

To conclude, for the TPMS structures studied here and for other related porous structures, 3D MultiJet printing associated with numerical homogenisation can be used in further studies for bone TE applications with tailored requirements.

ORCID

A. P. G. Castro http://orcid.org/0000-0002-6130-0408
R. B. Ruben http://orcid.org/0000-0002-5407-0579
J. M. Guedes http://orcid.org/0000-0001-9364-5059
P. R. Fernandes http://orcid.org/0000-0001-8458-096X

References

3D Systems. 2017. MultiJet Plastic Printers VisiJet ® M3 Advanced Plastics. Rock Hill, SC: 3D Systems.

Almeida HA, Bártolo PJ. 2014. Design of tissue engineering scaffolds based on hyperbolic surfaces: structural numerical evaluation. Med Eng Phys. 36:1033–1040.

ASTM International. 2002. ASTM D695 - 02a: standard test method for compressive properties of rigid plastics. West Conshohocken, PA: ASTM International.

Balabanian F, Sant'Ana da Silva E, Pedrini H. 2017. Image thresholding improved by global optimization methods. *Appl Artif Intell.* 31:197–208.

Barabaschi GDG, Manoharan V. 2015. Engineering mineralized and load bearing tissues. Adv Exp Med Biol. 881: 79–94.

Blanquer SBG, Werner M, Hannula M, Sharifi S, Lajoinie GPR, Eglin D, Hyttinen J, Poot AA, Grijpma DW. 2017. Surface curvature in triply-periodic minimal surface architectures as a distinct design parameter in preparing advanced tissue engineering scaffolds. *Biofabrication.* 9:025001.

Bobbert FSL, Lietaert K, Eftekhari AA, Pouran B, Ahmadi SM, Weinans H, Zadpoor AA. 2017. Additively manufactured metallic porous biomaterials based on minimal surfaces: A unique combination of topological, mechanical, and mass transport properties. Acta Biomater. 53: 572–584.

Boccaccio A. 2011. Finite Element Method (FEM), Mechanobiology and Biomimetic Scaffolds in Bone Tissue Engineering. Int J Biol Sci. 7:112–132.

Campos Marin A, Lacroix D. 2015. The inter-sample structural variability of regular tissue-engineered scaffolds significantly affects the micromechanical local cell environment. Interface Focus. 5:20140097–20140097.

Castilho M, Pires I, Gouveia B, Rodrigues J. 2011. Structural evaluation of scaffolds prototypes produced by three-dimensional printing. Int J Adv Manuf Technol. 56:561–569.

Castro APG, Lacroix D. 2018. Micromechanical study of the load transfer in a polycaprolactone–collagen hybrid scaffold when subjected to unconfined and confined compression. Biomech Model Mechanobiol. 17:531–541.

Coelho PG, Hollister SJ, Flanagan CL, Fernandes PR. 2015. Bioresorbable scaffolds for bone tissue engineering: optimal design, fabrication, mechanical testing and scale-size effects analysis. Med Eng Phys. 37:287–296.

Dinis JC, Morais TF, Amorim PHJ, Ruben RB, Almeida HA, Inforçati PN, Bártolo PJ, Silva JVL. 2014. Open source software for the automatic design of scaffold structures for tissue engineering applications. Procedia Technol. 16:1542–1547.

Eshraghi S, Das S. 2012. Micromechanical finite-element modeling and experimental characterization of the compressive mechanical properties of polycaprolactone-hydroxyapatite composite scaffolds prepared by selective laser sintering for bone tissue engineering. Acta Biomater. 8:3138–3143.

Feng J, Fu J, Shang C, Lin Z, Li B. 2018. Porous scaffold design by solid T-splines and triply periodic minimal surfaces. Comput Methods Appl Mech Eng. 336:333–352.

Gauvin R, Chen Y-C, Lee JW, Soman P, Zorlutuna P, Nichol JW, Bae H, Chen S, Khademhosseini A. 2012. Microfabrication of complex porous tissue engineering scaffolds using 3D projection stereolithography. Biomaterials. 33:3824–3834.

Giannitelli SM, Accoto D, Trombetta M, Rainer A. 2014. Current trends in the design of scaffolds for computer-aided tissue engineering. Acta Biomater. 10:580–594.

Guedes JM, Kikuchi N. 1990. Preprocessing and postprocessing for materials based on the homogenization method with adaptive finite element methods. Comput Methods Appl Mech Eng. 83:143–198.

Hollister SJ, Flanagan CL, Morrison RJ, Patel JJ, Wheeler MB, Edwards SP, Green GE. 2016. Integrating image-based design and 3D biomaterial printing to create patient specific devices within a design control framework for clinical translation. ACS Biomater Sci Eng. 2:1827–1836.

Hollister SJ, Murphy WL. 2011. Scaffold translation: barriers between concept and clinic. Tissue Eng Part B Rev. 17:459–474.

Kapfer SC, Hyde ST, Mecke K, Arns CH, Schröder-Turk GE. 2011. Minimal surface scaffold designs for tissue engineering. Biomaterials. 32:6875–6882.

Lakatos É, Magyar L, Bojtár I. 2014. Material properties of the mandibular trabecular bone. J Med Eng. 2014:470539.

Lu T, Li Y, Chen T. 2013. Techniques for fabrication and construction of three-dimensional scaffolds for tissue engineering. Int J Nanomed. 8:337–350.

Melchels FPW, Tonnarelli B, Olivares AL, Martin I, Lacroix D, Feijen J, Wendt DJ, Grijpma DW. 2011. The influence of the scaffold design on the distribution of adhering cells after perfusion cell seeding. Biomaterials. 32: 2878–2884.

Montazerian H, Davoodi E, Asadi-Eydivand M, Kadkhodapour J, Solati-Hashjin M. 2017. Porous scaffold internal architecture design based on minimal surfaces: a compromise between permeability and elastic properties. Mater Des. 126:98–114.

Nyma A, Kang M, Kwon Y-K, Kim C-H, Kim J-M. 2012. A hybrid technique for medical image segmentation. J Biomed Biotechnol. 2012:1–7.

O'Brien FJ, Harley BA, Waller MA, Yannas I V, Gibson LJ, Prendergast PJ. 2007. The effect of pore size on permeability and cell attachment in collagen scaffolds for tissue engineering. Technol Heal Care. 15:3–17.

Olivares AL, Lacroix D. 2012. Simulation of cell seeding within a three-dimensional porous scaffold: a fluid-particle analysis. Tissue Eng Part C Methods. 18:624–31.

Papantoniou I, Guyot Y, Sonnaert M, Kerckhofs G, Luyten FP, Geris L, Schrooten J. 2014. Spatial optimization in perfusion bioreactors improves bone tissue-engineered construct quality attributes. Biotechnol Bioeng. 111:2560–2570.

Rahbari A, Montazerian H, Davoodi E, Homayoonfar S. 2016. Predicting permeability of regular tissue engineering scaffolds: scaling analysis of pore architecture, scaffold length, and fluid flow rate effects. Comput Methods Biomech Biomed Engin. 5842:1–11.

Rajagopalan S, Robb RA. 2006. Schwarz meets Schwann: design and fabrication of biomorphic and durataxic tissue engineering scaffolds. Med Image Anal. 10:693–712.

Rodrigues HC, Coelho PG, Fernandes PR. 2011. Multiscale modelling of bone tissue - remodelling and application to scaffold design. Comput Methods Appl Sci. 20:15–33.

Sochol RD, Sweet E, Glick CC, Venkatesh S, Avetisyan A, Ekman KF, Raulinaitis A, Tsai A, Wienkers A, Korner K, et al. 2016. 3D printed microfluidic circuitry via multijet-based additive manufacturing. Lab Chip. 16:668–678.

Speirs M, Van Hooreweder B, Van Humbeeck J, Kruth JP. 2017. Fatigue behaviour of NiTi shape memory alloy scaffolds produced by SLM, a unit cell design comparison. J Mech Behav Biomed Mater. 70:53–59.

Velasco MA, Lancheros Y, Garzón-Alvarado DA. 2016. Geometric and mechanical properties evaluation of scaffolds for bone tissue applications designing by a reaction-diffusion models and manufactured with a material jetting system. J Comput Des Eng. 3:385–397.

Viana T, Biscaia S, Almeida HA, Bártolo PJ. 2013. Permeability evaluation of lay-down patterns and pore size of PCL scaffolds. Procedia Eng. 59:255–262.

Webber MJ, Khan OF, Sydlik SA, Tang BC, Langer R. 2015. A perspective on the clinical translation of scaffolds for tissue engineering. Ann Biomed Eng. 43:641–56.

Wismer N, Grad S, Fortunato G, Ferguson SJ, Alini M, Eglin D. 2014. Biodegradable electrospun scaffolds for annulus fibrosus tissue engineering: effect of scaffold structure and composition on annulus fibrosus cells in vitro. Tissue Eng Part A. 20:672–82.

Yoo DJ. 2014. Advanced porous scaffold design using multi-void triply periodic minimal surface models with high surface area to volume ratios. Int J Precis Eng Manuf. 15:1657–1666.